Soft Matter

Dynamic Article Links

Cite this: *Soft Matter*, 2011, **7**, 4983

www.rsc.org/softmatter

PAPER

Correlation between fibrin network structure and mechanical properties: an experimental and computational analysis

Eunjung Kim,†[f] Oleg V. Kim,†[a] Kellie R. Machlus,[c] Xiaomin Liu,[b] Timur Kupaev,[a] Joshua Lioi,[a] Alisa S. Wolberg,[c] Danny Z. Chen,[b] Elliot D. Rosen,[d] Zhiliang Xu[a] and Mark Alber*[ae]

Received 22nd December 2010, Accepted 24th February 2011
DOI: 10.1039/c0sm01528h

Fibrin networks, with and without cells, formed under wild type and hemophilic conditions, have been synthesized, studied and compared. The three dimensional structure of each fibrin network was reconstructed from two-dimensional *z*-stacks of confocal microscopy sections using novel image analysis algorithms. These images were used to establish microstructure-based models for studying the relationship between the structural features and the mechanical properties of the fibrin networks. The mechanical properties were assessed by analyzing the networks' responses to uniaxial tensile and shear stresses, simulating the impact of blood flow on the fibrin network. The elasticity of the fiber network predicted by the model agrees well with prior experimental data. The change in the fibrin network alignment under applied strain and the elastic modulus values were calculated and compared with prior experimental data obtained in Ryan *et al.*, *Biophys. J.*, 2009, **77**, 2813. The model correctly predicts the network alignment under load and the result is in good agreement with the results obtained for small networks in Brown *et al.*, *Science*, 2009, **325**, 741. It was shown that a nonlinear worm-like chain model correctly predicted both the elastic properties of the networks and the alignment of the fibers as the clot sample is stretched.

1. Introduction

In past studies, many of the blood plasma protein components, blood cellular components, elements in the vessel wall and the blood flow hydrodynamic factors that are involved in the development of a hemostatic clot have been identified. In addition to *in vitro* analysis, the development of mice that are deficient in specific hemostatic components has enabled us to study the role of particular elements of hemostasis *in vivo*. An extensive review of the different experiments and models studying blood clot formation can be found in Diamond.[3]

An important area in coagulation research is the study of the structural stability of a blood clot, which has important medical consequences. For instance, an abnormal fibrin network can make thrombi overly resistant to degradation or too fragile.[4–8] Abnormally structured clots may also generate emboli that can lodge in critical organs, disrupting the blood flow with potentially fatal consequences.

The stability of clots is closely related to the fibrin network, which provides the structural support for a blood clot (see

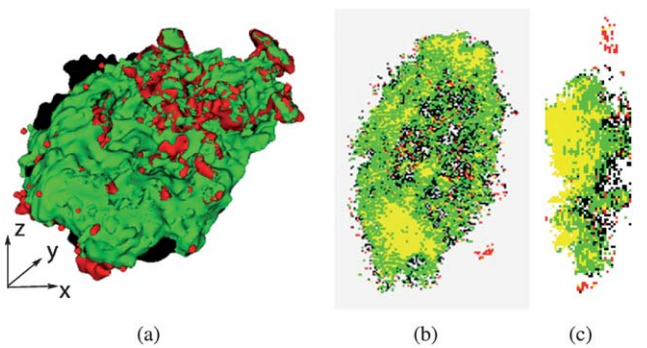

Fig. 1 A thrombus formed in a wild type mouse. (a) a three-dimensional reconstructed image of the clot; (b) a projection of the reconstructed image on the horizontal *xy* plane; and (c) a cross-section of the reconstructed image taken on the vertical *yz* plane within the blood clot. Platelets are in red; fibrin is in green; yellow is for a combination of platelets and fibrin; and black is for other blood cells. These images show that platelets are covered by the fiber network and the surface of the blood clot mainly consists of the fiber network.

[a]*Department of Applied and Computational Mathematics and Statistics, University of Notre Dame, IN, USA. E-mail: malber@nd.edu; Fax: +574 631 4822; Tel: +574 631 8371*
[b]*Department of Computer Science and Engineering, University of Notre Dame, Notre Dame, IN, USA*
[c]*Department of Pathology and Laboratory Medicine, University of North Carolina, USA*
[d]*Department of Medical and Molecular Genetics, Indiana University School of Medicine, Indianapolis, USA*
[e]*Department of Medicine, Indiana University School of Medicine, Indianapolis, USA*
[f]*Integrated Mathematical Oncology, Moffitt Cancer Center, 12902 Magnolia Drive, Tampa, FL, 33612, USA*
† These authors contributed equally to this work

Fig. 1). Following clot initiation, activated platelets release platelet activators and provide a membrane surface to support coagulation reactions. The procoagulant environment provided by the activated platelet surface enhances the production of thrombin, leading to further platelet activation and to fibrin polymerization. Thrombin converts fibrinogen to fibrin by cleaving fibrinopeptides from its central domain, exposing knobs that can then interact with holes at the ends of the molecules and generate protofibrils.[9,10] Protofibrils then grow and aggregate laterally to form fibers with twisted structures. Fibers aggregate with each other to a variable extent depending on the fibrinogen and thrombin concentrations and the ionic conditions to form fiber bundles, which branch to yield a three-dimensional network.[9–12] Since the fibrin network influences the shape, strength, flexibility and stability of clots,[9,10] the formation of the fiber network is crucial to clot function.

The mechanical properties of fibrin networks undergoing small deformations have been extensively studied using continuum models and inverse analysis of experimental data.[13,14] The values of the elastic modulus obtained using linear viscoelastic models are in the range 100–1000 Pa. The viscoelastic and elastic properties of an individual fiber have also been investigated.[2,15,16] It has been shown that individual fibers are relatively soft[15] and extraordinarily extensible.[16] Brown *et al.*[2] have shown that structural transitions of fibrin, including protein unfolding and water loss, allow the clot to be permeable and highly extensible.

A number of models have been developed to investigate the mechanical properties of biopolymer networks.[2,17–20] These studies associated the response of the fiber network to stress with two phenomena: the stiffening of fibers and their geometrical rearrangement, which is essentially determined by the flexibility of the individual fibers in the network. Therefore, network modeling must account for the behavior of individual fibers. For low strain, semi-flexible fiber and stiff fiber models were developed.[18,20] In the semi-flexible fiber models, the entropic stiffening was shown to be responsible for the network stiffening. In the stiff fiber models, the network stiffening was shown to result from a geometrical reorientation of fibers and from the bending at small strains and the enthalpic stretching at large strains. Both of these modeling approaches were successful in predicting the network behavior in the case of small strains.[17,18]

Recently, a model of small networks composed of 5–30 fibers was used to study the effects of fiber elasticity on the bulk properties of the small networks undergoing high deformation. The worm-like chain model is shown in Hudson *et al.*[21] to successfully describe force-extension relation of a single fibrin fiber. This model also shows that individual fibers play an important role in strengthening the entire network and that at large strains fibrin fibers composing the network display a nonlinear strain stiffening behavior. This nonlinear behavior results in the equitable strain stiffening redistribution in the network. As the fibers are stretched, the stiffer fibers distribute the load to the less strained fibers and thus, the strain concentration is reduced.

To the best of our knowledge, little attention has been paid to the study of alignment and fibrin stiffening of large fibrin networks at high strains. Moreover, although the network structure is hypothesized to play a key role in clot stability, most of the current studies do not take the detailed structure of the network into account when determining the bulk properties of the blood clot. Therefore, the main focus of this work was to delineate a complete picture of the behavior of the realistic fibrin clots consisting of a large number of fibers. This was done using computational models based on the geometric structures of the reconstructed 3D networks and the properties of the individual fibers.

Namely, we developed a mechanical model based on the microstructures of the realistic three-dimensional fibrin network, as well as the microscopic mechanics of single fibers, using a modeling strategy similar to that described by Hudson *et al.*[21] Specifically, 3D networks of fibrin clots comprised of thousands of fibers were considered. The clots were synthesized using normal platelet-poor plasma and hemophilic plasma to address the comparative strength properties of defective clots. We reconstructed the network structures from *z*-stacks of confocal microscopy images and used them in our model. The individual fibers were modeled by either a linear spring model or a nonlinear worm-like-chain model. The Young's modulus of the network was estimated as the ratio of the average force per unit area to the average yield strain.

Another result in the present paper is the development of an accurate image topology reconstruction method which allows one to reconstruct a fibrin network from a *z*-stack of 2D confocal microscopy images and to analyze the global structure of the network. This reconstruction method enables us to analyze various properties of the network, such as the density of the branch points and the width and length of the fiber segments. By quantifying the distribution of network neighbors, the most common type of connections is determined to be three-neighbor-type connections in all types of networks (see Fig. 5). Through 3D image reconstruction, a spatial nonconformity in the node and fibrin distribution for the network with cells was revealed. We observed that clots initiated by cellular procoagulant activity have preferential network node localization near cell surfaces, which is consistent with prior experimental data.[5]

Currently, determination of the number and length of fibers, as well as the number of branch points, in a fibrin network is done manually by analyzing scanning electron or laser scanning confocal micrographs of gels.[5,36] The algorithms described in this paper automate this process. We show that the results generated by the new image analysis algorithms agree well with the analysis done manually, and in addition this method is able to distinguish between fiber branch points and when two independent fibers cross one another in the gel.

The model and the image analysis algorithms were used for examining changes in the bulk modulus and scenarios mimicking the network interacting with blood flow by imposing strain on the fibrin network. This was done for a variety of experimentally obtained fibrin networks, including normal *versus* hemophilic plasma clots, clots with elevated prothrombin[22] and elevated fibrinogen,[36] low branching *versus* high branching networks, and fibrin networks with embedded cells *versus* networks without cells. We show that the elasticity of the fiber network predicted by the model agrees well with the experimental data. The model also correctly predicts the network alignment under load and it is in agreement with the results of Brown *et al.*[2]

For the networks we examined, networks formed with and without cells were found to reorient in a similar manner under an applied load. Hudson *et al.*[21] argued that the integrity of a fibrin network is largely determined by the maximum strain that the individual fibers can sustain and that network failure starts at the single fiber or branch point level. Our study confirms this finding for large realistic fiber clot networks. Therefore, the understanding of how a load is distributed within the network is critical to understanding network failure. Our results also underline the importance of having proper coupling in a fiber network of cells and mechanical network factors (*e.g.*, fiber density and fiber geometry) and its impact on the network strength. In particular, we showed that the average stiffness of fibrin networks with endothelial cells is about 2.6 times larger than that of networks without endothelial cells. Therefore, the interplay between these factors has profound consequences on clot stability.

The paper is organized as follows. Some biological background and a review of the current models are given in Section 1. Experimental details, image analysis, and our modeling methods based on recognizing microstructures of fibrin networks are described in detail in Section 2. The simulation results are presented in Section 3 and the conclusions are given in Section 4.

2. Methods

2.1. Modeling methodology

2.1.1. Network realization. Each network was simulated using nonlinear (or linear) mass-spring models. A fiber is represented by a bond between two rigid and freely rotating nodes from a 3D reconstructed image of a synthesized network (see below). The effect of stress applied by blood flow to the fiber network is modeled by imposing fixed boundary conditions on the bottom of the network ($z = 0$) and by applying strain to every node (Fig. 2). The geometry (diameter and free length) of each fiber was determined *via* image analysis.

2.1.2. Computational models. The elastic behavior of a network arises in the model from deformations of the elastic springs in the network, while the viscoelastic behavior is demonstrated when nodes propagate in a viscous flow. In what follows, we describe linear and nonlinear single fiber models and compare simulation results obtained using these two models. We show that the nonlinear fiber model has to be employed in order to take the strain stiffening of fibers into account.[21]

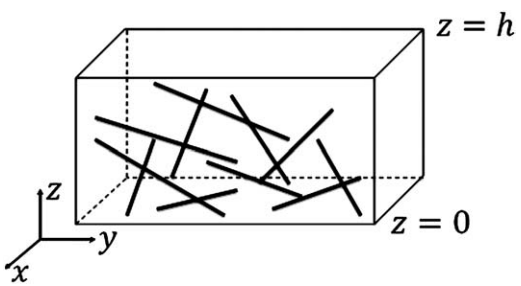

Fig. 2 Schematic of the computational domain and boundary conditions for the fibrin network. At $z = 0$: $\delta r_i(t) = 0$, at $z = h$: $\delta y_i(t) = \varepsilon y_i(0)$.

In the linear model, each fiber is represented by a linear spring, with a spring force given by

$$\boldsymbol{F}(\delta \boldsymbol{L}) = \kappa \delta \boldsymbol{L}, \tag{1}$$

where $\kappa = EA / L_0$ is the spring constant, E is the Young's modulus, A is the cross-sectional area of a fiber, and L_0 is the initial fiber length, and $\delta \boldsymbol{L}$ is the extension of a fiber. The Young's modulus is taken to be 14.5 MPa.[15]

Several recent theoretical models have been proposed to account for the strain stiffening of fibers.[17,21] Which of these models is the most applicable to a fibrin network depends on how flexible a fiber is compared to the mesh size of the network. Since the persistence length of the fiber is comparable to the mesh size or the distance between cross-links within the network, the strain stiffening in the fiber network naturally emerges from an entropic model, in particular, from an ideal worm-like chain model. This model has been successfully used for describing force-extension behavior of a fibrin fiber.[2,21] The stress-strain relation for a fiber is also represented in our model as a worm-like chain for a large strain in the form of the following governing equation

$$F = \frac{k_B T N}{P}\left[\frac{1}{4}\left(1 - \frac{\delta \boldsymbol{L}}{L_c}\right)^{-2} - \frac{1}{4} + \frac{\delta \boldsymbol{L}}{L_c}\right], \tag{2}$$

where k_B is the Boltzmann constant, T is the absolute temperature, N is the number of fibrin molecules making up a fiber, P is the persistence length, L_c is the contour length, and $\delta \boldsymbol{L}$ is the extension of a fiber (see Table 1). The governing equation for the ith connection node is given by $m_i \ddot{\boldsymbol{r}}_i = -\gamma \dot{\boldsymbol{r}}_i + \sum_j \boldsymbol{F}_{ij}$. Here, $\boldsymbol{F}_{ij}$ is the force acting along the fiber connecting the ith and the jth nodes and given by eqn (1) or (2), $\boldsymbol{r}_{ij}$ is the radius vector connecting the ith and jth nodes, and m_i is the mass of the ith node. The damping term was approximated using the Stokes force due to the interaction with the blood flow, $\gamma = 6\pi\mu r_f$, where, $\mu = 0.004$ Pa s[23] is the blood viscosity, and r_f is the radius of the node. A leapfrog algorithm was used to solve the system of ordinary differential equations governing the network of springs. After an incremental strain is applied during one time step, the system relaxes to its equilibrium, which is used as an initial condition for the next time step.

2.1.3. Determination of elastic properties. The volume average method has been used to examine the strength of a discrete network.[24–27] This method approximates the stress tensor as a finite sum of the product of the position and the traction exerted on the boundary, *i.e.*, $\sigma_{ij} = \frac{1}{V}\sum x_i \alpha_{kj} n_k$, where σ_{ij} is the network stress, V is the volume, α_{ij} is the fiber stress tensor and n_k is the kth component of the normal vector. The

Table 1 The parameter values used in the linear and nonlinear models. These values were taken from the work by Brown *et al.*[2]

Linear Model	Nonlinear Model
$E = 14.5$ MPa	$k_B = 1.38 \times 10^{-23}$ J K^{-1} $N = 1200$ $T = 300$ K $P = E\pi r^4 / k_B T$

finite approximation of the stress converges to the continuum stress tensor as the number of fibers on the boundary increases. Thus, this method may be especially useful for dense networks. However, our reconstructed fibrin network is relatively coarse. The density (number of fibers per unit volume 1 μm^3) is in the range from 0.013 μm^{-3} to 0.17 μm^{-3}. The density of the network is even smaller near the boundary and, thus, the stress determined by the volume average method, may not converge to a specific value. Therefore, rather than using the volume average method, the estimated stress of the network was calculated by summating the forces of the fibers on the network boundary to which the force was applied and the elastic modulus was determined as the ratio of the average force to the average strain, *i.e.*,

$$\lambda = \frac{\left(\sum F_i/A_i\right)_{i=1}^{M}}{\varepsilon} \quad (3)$$

where F_i is the normal component of the force acting on the ith fiber of thickness A_i, ε is the average strain, and M is the total number of fibers.

2.2. Experimental methods

2.2.1. Materials. Phosphatidylserine, phosphatidylcholine, and phosphatidylethanolamine were purchased from Avanti Polar Lipids (Alabaster, AL, USA). Corn trypsin inhibitor (CTI) and prothrombin were from Haematologic Technologies Inc. (Essex Junction, VT, USA). Fibrinogen was from Enzyme Research Labs (South Bend, IN). Cells (human umbilical vein endothelial cells) were purchased from Lonza and cultured as described.[28] Tumor necrosis factor alpha (TNFα) was from Millipore. AlexaFluor-488-labeled fibrinogen was prepared according to the manufacturers instructions [Invitrogen Corporation (Carlsbad, CA)]. The labeled fibrinogen contained 8 molecules of dye per fibrinogen molecule. The preparation was frozen in aliquots that were thawed only once at 37 °C before each experiment. Turbidity measurements on fibrin formed in the presence or absence of labeled fibrinogen demonstrated that the inclusion of labeled fibrinogen did not affect polymerization (data not shown). Phospholipid vesicles (15% phosphatidylserine, 41% phosphatidylcholine, 44% phosphatidylethanolamine) were prepared by extrusion.[29]

2.2.2. Plasma preparation. Blood was collected with informed consent under a protocol approved by the University of North Carolina Institutional Review Board. Whole blood was drawn into 3.2% citrated saline and corn trypsin inhibitor (18.5 $\mu g\ mL^{-1}$, final, to prevent contact activation) and centrifuged at 150*g* for 10 min. The upper layer (platelet-rich plasma) was centrifuged at 13 000*g* for 10 min to yield platelet-free plasma. Platelet-free plasma from at least 30 individuals with normal partial thromboplastin times were pooled to yield normal pooled platelet-free plasma (PFP). PFP was then used with or without additional exogenous prothrombin (spiked to 200% or 400%, final) or fibrinogen (spiked to 6 $mg\ mL^{-1}$ (200%), final). Hemophilia A plasma was purchased from HRF, Inc. (Raleigh, NC, USA).

2.2.3. Clot formation and laser scanning confocal microscopy. Clot formation in the absence of cells was initiated by the addition of calcium, phospholipid vesicles and tissue factor (16 mM, 4 μM and 1 pM, final, respectively) to plasma. Clot formation in the presence of cells was initiated by adding calcium to plasma and triggered by cellular tissue factor. Alexa-Fluor 488-labeled fibrinogen was included in each reaction as a trace molecule to visualize fibrin structure (10 μg/150 μL, final). Clots were allowed to form until turbidity reached a stable maximum in samples run in parallel, as described.[5,28] Formed clots were scanned with a Zeiss LSM5 Pascal laser scanning confocal microscope (Carl Zeiss, Inc) linked to a Zeiss Axiovert 200M microscope equipped with a Zeiss 63× 1.4 NA oil immersion plan apo-chromatic lens. The 488 nm line of a medium power multi-line argon ion laser was used for excitation and a 505–530 nm band-pass filter was used for emission. A computer equipped with Carl Zeiss software (v1.5) was used to operate the system. Optical sectioning was achieved by closing the pinhole in the front of the detector to one Airy unit. The zoom factor was 1. 30–60 optical sections (1024 × 1024 pixels each) in three randomly chosen locations were collected at 0.36 μm intervals in the z axis. Optical resolution was 0.14 μm in the xy plane and 0.5 μm on the z axis. The sectioning interval in z was smaller than the calculated z axis optical section resolution to achieve Nyquest sampling in z based on the Zeiss software calculation. No correction was made for refractive index mismatch.

2.3. Image analysis

The goal of our image segmentation and analysis algorithms was to identify and segment the fibrin network using 3D images of networks reconstructed from z-stacks of confocal microscopy images, and to extract the global structure of the network. The idea was to compute the 3D medial axis/centerline preserving the topology of the original network. As a result, we obtained a one-voxel-wide centerline, in which the branch points and other structural information could be computed. Based on the centerline, we were able to analyze various properties of the network, such as the density of the branch points, the width and length of the fiber segments, the pore size, *etc.* Furthermore, the topology of the network could be simplified and modeled by a 3D graph, in which the vertices represent the branch points or end points of the fibrin network, and the edges connecting pairs of vertices correspond to the fiber segments between consecutive branch points (or end points) in the original network. The graph representation of the network and the measurements of the network properties were then used as input for the computational modeling and 3D reconstruction.

2.3.1. Methodology of image analysis. Our image segmentation and analysis algorithm consisted of five main steps, described below.

Segmentation. We first needed to identify the fibrin network in the input image and separate it from the image background. We used the 3D region growing method[30] with global thresholding to identify the voxels belonging to the sought fibrin network, resulting in a binary image in which the fiber was labeled 1 and the background was labeled 0 (see Fig. 3). The algorithm

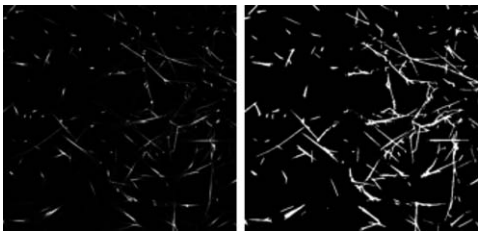

Fig. 3 Image segmentation results. Original image (left) and segmented image (right).

repeatedly takes a seed point as an input, and iteratively includes the points in its neighborhood until no points beyond the threshold are left. The seed points were determined by selecting the points with the maximal intensity values in the image.

3D thinning. The 3D medial axis/skeleton of a target 3D object is a concrete representation of the overall structure of the object. Given the surface of a target object, its 3D medial axis or skeleton is a set of points, each of which has at least two distinct nearest points on the surface. Although an accurate computation of the 3D medial axis is a difficult task, various approximation algorithms based on a Voronoi diagram, distance transformation, or thinning have been proposed for computing the medial axis. Our method is based on the 3D thinning algorithm, which allows for a fast computation in digital images and results in a one-voxel-wide centerline.[31] The centerline preserves the same anatomy of the original network and provides useful structural information, such as the branch points, the length of each network segment, *etc.* In each iteration, the thinning algorithm checks whether a voxel is removable from the remaining voxels, until no more changes can be made. Any voxel to be removed must satisfy the following conditions:

- The voxel is on the current object surface;
- The voxel is not at the end of a network segment;
- Deletion of the voxel does not change the Euler characteristic (*i.e.*, does not create new holes in the image);
- The voxel is a simple point, so that its deletion does not change the number of connected object components in the image.

Branch points identification. After the centerline is extracted, we labeled each centerline point according to the number of centerline points in its neighborhood and identified the network branch points based on their labels. An end point has only one neighbor in its 26-neighborhood in the 3D image, a non-branch point has two neighbors, and a branch point has three or more neighbors. In Fig. 4, the branch points are marked by red and the end points are marked by blue.

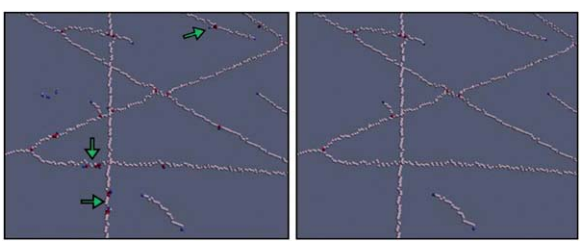

Fig. 4 The 3D centerline of the fibrin network: The centerline before pruning (left) and the centerline after pruning (right). The arrows are pointing at some false branches before pruning.

Pruning. A well known inherent problem of the medial axis is its sensitivity to local changes on the object's surface. That is, even a small pertubation on the surface may cause a significantly different medial axis structure. As a result, a noticeable set of false short branches exists in the centerline, which affects the accuracy of our analysis of the density of branch points. A number of pruning methods have been proposed to prune these undesired medial axis features, but none of them can completely solve our problem. Most pruning methods rely on a significance measure for each of the axis/centerline points.[32] In our experiments, the pruning is closely related to the identification of branch points (see Fig. 4). We observe that although a small perturbation of the surface may introduce undesired branches on the inner medial axis, it does not affect the outer medial axis much. The outer medial axis of a non-branching fiber with a small perturbation is much farther away from the object boundary than that of a branching fiber. Hence, we pruned out the false branches based on their lengths and the distance from the branch point to the outer medial axis. The latter can be computed by a method based on Delaunay triangulation.[33] Only the branch points that are within a certain distance to the outer medial axis are preserved.

Network analysis and simplification. Using both the segmented network and its centerline, we are able to analyze the network structure and produce a graphical representation of the network. A depth-first search (DFS) is performed on the centerline to traverse each branch point and end point and obtain its geometric position. An edge is created in the graph to connect two vertices (branch points and/or end points) if they can be reached from each other through a path of non-branch points. To compute the thickness of each fiber segment, we use a plane at each centerline point orthogonal to the fiber segment and count the connected object voxels around that centerline point within the plane. As a result, a graph is generated for the network. The vertices of the graph represent the branch points and end points, and the edges of the graph represent the fiber segments between consecutive branch points and end points (with known average fiber thickness). This simplified structure also makes possible a 3D reconstruction that presents the 3D structure of the network and allows for fast manipulation of the network (rotation, zoom in and out, *etc*).

3. Results

In this section, we first present the results of analyzing fiber networks that do not sustain any load. Next, the elasticity of various networks is given. Finally, we show how networks reorient under loads, which relates the network structure to its mechanical properties.

3.1. Fibrin networks analysis

We examined the fibrin structure from 3D reconstructed images of clots obtained using the experimental approach described in Section 2.3.1. Results of the image analysis were used to recreate

a three-dimensional network and to perform its structural analysis. We studied the inter-fibrin network differences in structure by counting the number of branch points, estimating the average thickness and computing the densities of the nodes as a function of the radial distance from the cells.

Analysis of peculiarities and data comparison of fibrin networks with and without cells and of hemophilic networks were performed (see Table 3) to assess both feasible structural similarities and differences.

Clots prepared from normal poor-platelet plasma (NPP) or hemophilic poor-platelet plasma (HPP), triggered by lipidated tissue factor, unstimulated cells (indicated by ^{C}), or cells stimulated by tumor necrosis factor alpha TNFα (indicated by $^{TNF\alpha\text{-}C}$) were used. The clotting activity was changed in NPP by adding prothrombin to 200% or 400% of normal levels (indicated by $_{200II}$ and $_{400II}$), or fibrinogen to 6 mg mL^{-1} (200% of the normal level) (indicated by $_{200Fgn}$). The network structures of clots produced under these conditions have previously been well-characterized,[1,5,22,28,34-36] and these studies provided a range of structures suitable for developing our algorithms. Briefly, both elevated prothrombin and elevated fibrinogen increase the network density relative to NPP.[1,5,22,36] Using cell monolayers to initiate clotting produces clots with denser networks near the cell surface than distal to the cell surface.[5,28] TNFα-stimulated cells have a higher procoagulant activity than unstimulated cells and produce denser networks than unstimulated cells.[28,36] Hemophilic clots contain a coarser network of thicker fibers than normal clots.[34,35] Under the experimental conditions used, clots formed with unstimulated cells or lipidated tissue factor have close mean density values, whereas clots formed with TNFα-stimulated cells have on average 2.3 times higher densities than NPP sample clots (2.2, 2.9, and 1.8 times for 0%, 200%, and 400% of prothrombin concentration, respectively).

The number of neighbors for each network node was calculated. The distribution of neighboring nodes for all types of networks was found to be quite similar having a maximum of $n = 3$ neighbors. In this most common connection type, the node is conjugated with three other nodes (Fig. 5).

In networks formed without cells the number of nodes with 3 neighbors comprises 53–57% of the total number of nodes. The same index for hemophilic network is 51%. Four-neighbors connection type nodes comprise 13–16% of the total number of nodes in the NPP samples, 13–18% in the NPP samples with cells (joint stimulated and unstimulated cells), and 10% in the hemophilic sample. Two-neighbors connection type nodes comprise only 1% of the total number of nodes. One neighbor nodes comprise 20–28% (no cells) and 35% (hemophilic) of all nodes.

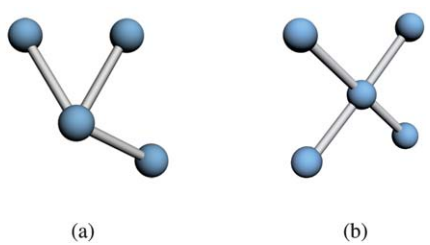

Fig. 5 Some types of network connections: (a) the most common three-nodes connection type and (b) the four-nodes connection type.

The averaged distributions of neighbors are presented in Fig. 6, in which histograms for the networks formed with cells (a), without cells (b), and from hemophilic plasma (c) are shown. Here, (a) presents stimulated and unstimulated cells samples together, (b) presents all no cells samples (see Table 3).

Two approaches were used to determine the network density. In the first approach the network density was calculated by counting the total number of branch points in the sample and dividing this by the sample volume. The second approach used a previously published method,[5] in which the network density was manually quantified and analyzed using commercial software ImageJ (version 1.37v, National Institute of Health). Briefly, a random grid of 2-pixel crosses was placed on individual slices and the density was determined by counting fibers intersecting the middle of the crosses, divided by the total number of crosses. Crosses placed over cells were subtracted from the total number of crosses. Table 2 shows the comparison of the two methods, as the nondimensional relative network densities for the studied samples are presented. These nondimensional values were calculated by dividing the actual densities by the density of the NPP sample. The values from these two methods are linearly and positively correlated ($R = 0.923$). However, method I is less time consuming and, because it measures all fibers rather than only a sample, it is expected to be more accurate than method II.[5]

We also found that the hemophilic clots contain thicker than normal fibers, which is consistent with the findings from scanning electron microscopy.[34] It should be noted the the absolute diameters measured by scanning electron microscopy are thinner than they are in hydrated clots, such as those imaged by confocal microscopy. This is partially because the resolution of confocal microscopy is not high enough to resolve small length scales. Due to the large deviation in the measured fiber diameters, we could not correlate the thickness and the thrombin concentration. In general, clots produced with higher thrombin concentrations would be expected to have thinner fibers.[22]

The results in Table 2 and Table 3 show that the network density increases with increasing concentration of prothrombin

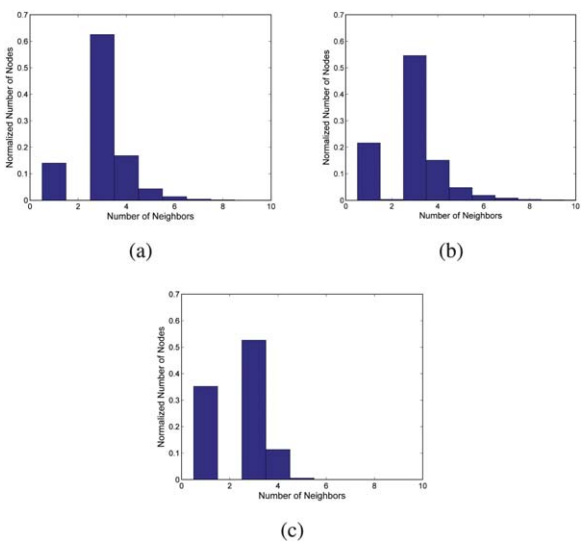

Fig. 6 Distribution of the number of neighbors in networks (a) of NPP type with cells, (b) of NPP type without cells, and (c) obtained from hemophilic plasma.

Table 2 Average relative network densities evaluated by two approaches: a published method[5] (left column), and a computational method for network data analysis (right column)

	Network Density n/n_{NPP}	
Sample	Method I	Method II
No cells		
NPP (Normal Pooled Plasma)	1	1
NPP_{400II}	1.5	1.9
NPP_{200Fgn}	1.8	2.5
Unstimulated cells		
NPP^{C}	0.7	0.3
$NPP^{C}{}_{200II}$	1.5	1.2
$NPP^{C}{}_{400II}$	1.9	2.1
TNFα-stimulated cells		
$NPP^{TNFα\text{-}C}$	1.8	2.2
$NPP^{TNFα\text{-}C}{}_{200II}$	2.5	2.33
$NPP^{TNFα\text{-}C}{}_{400II}$	3.1	3.3

and fibrinogen, which is consistent with prior experimental results.[1,5,22,36] In addition, consistent with experimental work by Campbell *et al.*,[28] the network density in clots produced by TNFα-stimulated cells is higher compared to that in clots produced by unstimulated cells.

The spatial distribution of the network nodes was also determined. For this purpose each sample was divided into 29 equal layers in the z direction and the number of nodes in each layer was counted, enabling one to calculate the average node density and the number of nodes per unit volume (nodes cm^{-3}) as a function of the z coordinate. Here, $z = 0$ corresponds to the bottom of the well, the z axis is directed toward the sample surface, and x and y form the coordinate system of the layer. The spatial distributions of the node density for clots produced by homogeneously distributed soluble tissue factor in plasma are shown in Fig. 7(a). It can be seen that the nodes are quite uniformly distributed along the z axis. In contrast, the node density of the networks produced by cellular tissue factor, which localized procoagulant activity to the cell surface, gradually decreases as z increases (Fig. 7(b)). Such a difference in the network node density distributions can be attributed to clotting in the sample volume, due to diffusion of thrombin from the cellular surface into the plasma medium.[5] The node density averaged in the z direction through the 3.3 μm thick layer is

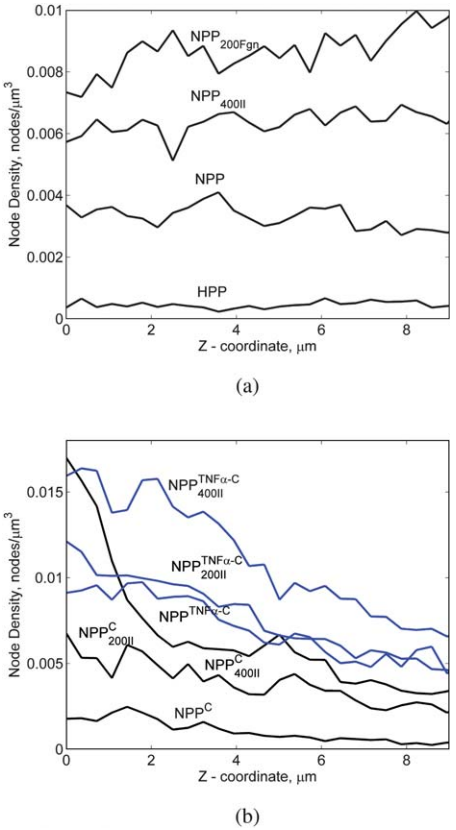

Fig. 7 The number of nodes per layer for (a) the networks formed in normal plasma and hemophilic plasma, in the absence of cells and (b) the networks formed in normal plasma with cells.

shown in Fig. 8. As seen from the Figs 8(c) and (d), the nodes are more densely populated near cells resulting in a non-uniform node density distribution (Fig. 7(b)). For comparison, the node densities for the network without cells and for the hemophilic type network are presented in Figs 8(b) and (a), respectively. It can be clearly seen that the network without cells displayed a rather uniform structure. The hemophilic network displays a much more penetrable structure than the clots produced in NPP, which is consistent with previous experimental findings.[35] This increased permeability is thought to reduce the ability of

Table 3 A summary of the quantitative measurements of the fibrin networks

Sample	Number of branch points	Average fibrin diameter (μm) (mean ± SD)	Average fibrin length, μm (mean ± SD)
HPP (Hemophilic)	759	1.94 ± 1.32	5.98 ± 5.51
No cells			
NPP (Normal Pooled Plasma)	5422	1.54 ± 1.00	2.86 ± 2.51
NPP_{400II}	10 123	1.47 ± 0.89	2.30 ± 1.82
NPP_{200Fgn}	13 604	1.38 ± 0.88	2.03 ± 1.60
Unstimulated cells			
NPP^{C}	1855	2.12 ± 1.63	4.16 ± 3.61
NPP^{C}_{200II}	6610	2.41 ± 1.73	2.95 ± 2.40
NPP^{C}_{400II}	11 406	2.35 ± 1.65	2.61 ± 2.11
TNFα-stimulated cells			
$NPP^{TNFα\text{-}C}$	11 938	1.78 ± 1.15	2.60 ± 1.83
$NPP^{TNFα\text{-}C}_{200II}$	12 675	1.82 ± 1.28	2.54 ± 1.92
$NPP^{TNFα\text{-}C}_{400II}$	18 138	2.46 ± 1.78	1.98 ± 1.49

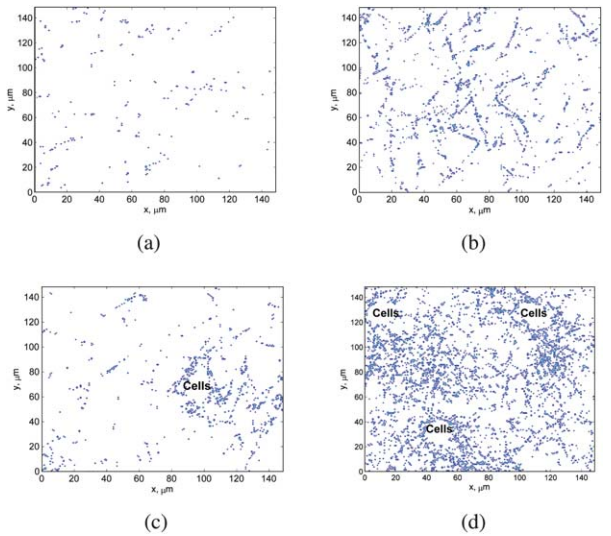

Fig. 8 Branch point density distributions for different types of networks: (a) the hemophilic type network (HPP), (b) the fibrin network from normal plasma containing no cells (NPP), (c) the fibrin network with unstimulated cells NPP^{C}, (d) the fibrin network with stimulated cells $NPP^{TNF\alpha\text{-}C}$.

these clots to prevent bleeding at the sites of injury in hemophilic patients.[35]

3.2. Elastic properties of fibrin network

The accuracy of the models was validated by comparisons to experimental data[1] for randomly generated fibrin networks. A set of random networks was generated based on quantitative measurements in ref. 1 (see Table 4). The Young's modulus of individual fibers in the model was varied from 1 Mpa to 15 Mpa, when 5–25% of the strain was applied to the network. The estimated modulus values were compared with the storage modulus G' in ref. 1, since the loss modulus (G'') was much smaller than G', using the ratio $\frac{G''}{G'} \leq 0.04$. The model predictions and experimental data are in good agreement for using the worm-like chain nonlinear model, while the linear model fails to predict the experimentally measured values (See Table 4). Here, the storage modulus, G', and the loss modulus, G'', represent the elastic and the viscous portions of the complex modulus $G = G' + G'' = \tau''/\gamma + \tau'/\gamma$, where τ' and τ'' are the viscous and elastic stresses, and γ is the maximum strain.

Once the accuracy of the model was validated, the model was employed to estimate the modulus of the reconstructed networks, as described in the previous method section. Table 5 summarizes the computed bulk elastic modulus for all of the networks. The average stiffness of the networks with cells ($<\lambda_I> = 194.5$ Pa) was 2.6 times higher than that without cells ($<\lambda_{II}> = 74.3$ Pa). The $NPP^{TNF\alpha\text{-}C}{}_{400II}$ sample was found to have the highest stiffness and therefore can be considered to have the most stable structure among all of the samples. These findings are in agreement with previous experimental studies,[5] which suggest that thrombin generation on the cell surface modulates the three-dimensional structure and the stability of the clot.

The stiffness of the hemophilic network was 10 times lower than the average stiffness of the networks produced from normal plasma. This is consistent with experimental data showing a reduced elastic modulus of the hemophilic clots compared to the normal clots.[37]

Table 5 The calculated elastic modulus of different fibrin networks

Sample	λ, Pa
HPP	7
NPP	23
NPP_{400II}	97
NPP_{200II}	123
NPP^{C}	167
NPP^{C}_{200II}	170
NPP^{C}_{400II}	175
$NPP^{TNF\alpha\text{-}C}$	161
$NPP^{TNF\alpha\text{-}C}_{200II}$	130
$NPP^{TNF\alpha\text{-}C}_{400II}$	363

3.3. Fibrin network orientation parameter

Hydrodynamic stresses, such as those due to blood flow, can deform the fibrin network. The orientation of the fibers and alterations in the fiber density affect the physical properties of the clot.

In a recent work by Whittaker and Przyklenk[38] the fibrin fiber bundle orientation was used to assess thrombus structure. Three different types of clots were analyzed: clots formed *in vitro*, clots formed within coronary arteries after injury to the tunica media and development of stenosis, and clots from luminal thrombi obtained six weeks after surgical induction of an abdominal aortic aneurysm and subsequent placement of embolic coils in pigs. The two-dimensional fiber bundle orientation was determined by measuring the angular deviation: *in vitro* 28.7°, in coronary samples 18.6°, and in aortic samples 4.4°. Assuming the network to be two-dimensional, the corresponding orientation parameters (defined below) were 0.54, 0.8, and 0.99. Under

Table 4 Comparison of numerical and experimental values [1] of network elastic modulus

Sample[1]	Fibrin thickness, nm	Number of branch points	G', Pa (exp. reports)[1]	λ, Pa (linear model)	λ, Pa (nonlinear model)
A	72	26	0–10	26 980	7
B	61	21	0–50	18 100	71
C	46	80	100–150	72 832	116
E	44	137	25–50	52 564	18
F	85	11	50–100	10 170	136
I	69	7.7	200–300	3030	69

no-load conditions the orientation parameter of the *in vitro* synthesized fibrin clots was close to 0.1.[2]

Thus, the orientation of the fibers varies widely and depends on the clotting conditions, such as the external loads, active surfaces, the presence of cells, *etc.* One of the factors strongly influencing the fiber orientation is stress on the fiber surfaces produced by blood flow.[39] In the present study, the effect of the blood flow was approximated by a uniformly distributed strain load across the sample network. The effect of the applied strain on the network alignment was studied numerically for three different types of clot samples; HPP, NPP, and NPP^C (see Table 3 and Table 5). The fibrin network orientation parameter was used to quantitatively describe the fibrin alignment along the ith coordinate axis, where $i = x,y,z$. This parameter is defined here as $P_i = 2\langle\cos^2\theta_i\rangle - 1$, where θ_i is the direction angle between a fiber and one of the ith axes, and averaging is done over all fiber segments composing the sample. According to the given definition of the parameter P_i, it ranges from -1 to 1 and allows the assessment of a three-dimensional network alignment, with respect to the coordinate axes. If network fibers are randomly oriented with respect to the ith direction, then $Pi = 0$. For fibers oriented perpendicular to the ith direction, $P_i = -1$. If the network is perfectly aligned along the ith direction, $P_i = 1$.

The structure of the initially unstressed fibrin clots was found to exhibit anisotropic alignment. For example, for the hemophilic sample the orientational parameter was $\boldsymbol{P} = (P_x,P_y,P_z) = (-0.241, -0.323, -0.92)$, for the NPP sample, $\boldsymbol{P} = (-0.438, -0.29, -0.863)$, and for the NPP^C sample, $\boldsymbol{P} = (-0.38, -0.183, -0.91)$. The values of P_z are close to -1, which probably results from the fact that fibrin clot samples were prepared as thin layers so that most of the fibers aligned in the xy plane.

When strain was applied along one of the ith directions, the fibers began to align and the fibrin network orientation parameter gradually increased from its initial value to some asymptote as seen in Fig. 9 and 10. For comparison, experimental data from Brown *et al.*[2] are shown in Fig. 10. Although experiments were done with fibrin networks with different structural topologies, the model correctly predicts the range of the orientation parameter.

The analysis of the network orientation of clots formed *in vitro* revealed that although the fibrin fibers were disorganized, their orientations were not random. The fibers were found to be generally aligned in parallel to the bottom of the well, and to have nonzero orientation components P_x and P_y. It should be noted that in experimental vascular clots the mean orientation of fibers is in the circumferential direction within the vessel.[38] This is the result of shear stresses present during fiber formation.[39] The alignment of the fibers studied here, under no flow conditions, results from some other mechanism, possibly an interaction with the glass surface of the well.

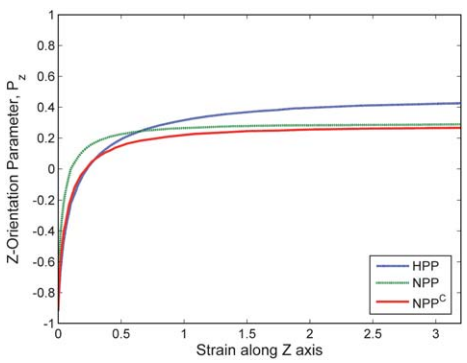

Fig. 9 The orientation parameter P_z as a function of the applied strain.

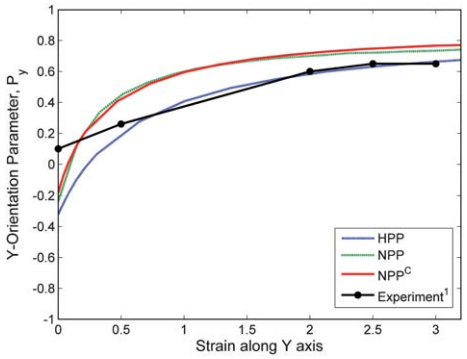

Fig. 10 The orientation parameter P_y as a function of the applied strain.

4. Conclusions

The structural features and mechanical properties of three types of fibrin networks were studied: networks formed from normal plasma with and without cells, and from plasma from a hemophilic patient.

A multistep approach was developed for the reconstruction of a three-dimensional network structure from experimental images to quantify the structural properties of fibrin networks. An algorithm was developed that significantly speeds up the image analysis. It was found that all types of networks exhibit a similar distribution of neighbors with three-neighbor connections being the most common. Spatial non-uniformity in fiber and node distributions was found in networks with cells, likely attributable to localized expression of the procoagulant on the cell surface.[5,28]

The mechanical model based on the microstructures within the network extends the prior model for small networks[21] and enables one to calculate the bulk properties of the network. The nonlinear worm-like chain model of individual fibers correctly predicts both the elastic properties of the networks and the alignment of the fibers as the clot sample is stretched. The predicted results of the network alignment were shown to be in agreement with experimental data.[2] Therefore the developed model can be used to interpret experimental results as well as to design further experiments on determining fibrin clot structural changes under different mechanical loads.

While blood clots made of platelets and a fibrin network prevent bleeding after a break in blood vessels, pathological clotting within vessels (thrombosis) generates thrombi that can occlude vessels or generate emboli that may lodge in and restrict blood flow to critical tissues. An overly stable clot which consists of a dense fibrin network and is less permeable may be resistant to fibrin lysis. Brown *et al.*[2] studied fibrin structures to address how fibrin clots are both permeable and extensible by examining molecules, single fibers and whole clots. The protein unfolding explains how a fiber behaves as a linear spring with a strain of 1.2 and starts to display strain hardening afterwards. We

interpolated this phenomenon by applying a worm-like chain model developed by Hudson *et al.*[21] to represent a single fiber. Our study confirmed the importance of taking into account protein unfolding and nonlinear elasticity of single fibers.

Our simulations show that the average stiffness of a hemophilic fibrin network sample is about 10 times smaller than the average stiffness of normal fibrin networks. The average stiffness of fibrin networks formed with cells is about 2.6 times larger than the average stiffness of fibrin networks formed without cells. Differences in stiffness can partially be attributed to the structural differences in networks at the macroscale.

Fibrin networks generated from the hemophilic plasma samples are more sparse than networks formed from wild type samples. The model predicts such networks to be less resistant to shear stress generated by blood flow, which is consistent with clot instability seen in hemophiliac patients.

Our results show that differences in mechanical properties of different fibrin networks can be partially explained by the structural differences in networks at the macroscale. However, if one could understand how the rate of fibrin generation is affected by changes in coagulation activity and how fibrin fibers form at the molecular level, it would be possible to predict the mechanical properties of fibrin networks formed in individuals with particular coagulation factor profiles. The ability to determine the properties of fibrin networks would have significant biomedical value, enabling one to better assess thrombotic or hemorrhagic risk and the response to therapeutic interventions.

Acknowledgements

This research was supported in part by NSF grants DMS-0800612, CCF-0515203 and CCF-0916606, NIH grants HL073750-01A1, and HL094740, the American Heart Association (10PRE3720011), the INGEN Initiative to Indiana University School of Medicine, and a graduate fellowship from the Center for Applied Mathematics, University of Notre Dame. Mark Alber and Oleg Kim were partially funded by the Gerber Foundation. Timur Kupaev was supported by NSF grant BCS-0826958. We thank Chris Sweet for the help with visualization of the structure of the reconstructed fiber networks and code implementation.

References

1 F. A. Ryan, L. F. Mockros, J. W. Weisel and L. Lorand, *Biophys. J.*, 1999, **77**, 2813–2826.
2 A. E. X. Brown, R. I. Litvinov, D. E. Discher, P. K. Purohit and J. W. Weisel, *Science*, 2009, **325**, 741–744.
3 S. L. Diamond, *J. Thromb. Haemost.*, 2009, (Suppl 1), 177–180.
4 H. Bounameaux, *Lancet*, 2000, **356**, 182–183.
5 R. A. Campbell, K. A. Overmyer, C. R. Bagnell and A. S. Wolberg, *Arterioscler., Thromb., Vasc. Biol.*, 2008, **28**, 2247–2254.
6 J. P. Collet, Y. Allali, C. Lesty, M. L. Tanguy, J. Silvain, A. Ankri, B. Blanchet, R. Dumaine, J. Gianetti, L. Payot, J. W. Weisel and G. Montalescot, *Arterioscler., Thromb., Vasc. Biol.*, 2006, **26**, 2567–2573.
7 K. Fatah, A. Hamsten, B. Blomback and M. Blomback, *Thromb. Haemost.*, 1992, **68**, 130–135.
8 K. Fatah, A. Silveira, P. Tornvall, F. Karpe, M. Blomback and A. Hamsten, *Thromb Haemost.*, 1996, **76**, 535–540.
9 J. W. Weisel, *J. Thromb. Haemost.*, 2007, **5**, 116–124.
10 S. T. Lord, *Curr. Opin. Hematol.*, 2007, **14**, 236–241.
11 J. W. Weisel, *Adv. Protein Chem.*, 2005, **70**, 247–299.
12 A. S. Wolberg, *Blood Reviews*, 2007, **21**, 131–142.
13 S. L. Diamond, *Annu. Rev. Biomed. Eng.*, 1999, **1**, 427–462.
14 J. Noailly, H. Van Oosterwyck, W. Wilson, T. M. Quinn and K. Ito, *J. Biomech.*, 2008, **41**, 3265–3269.
15 J.-P. Collet, H. Shuman, R. E. Ledger, S. Lee and J. W. Weisel, *Proc. Natl. Acad. Sci. U. S. A.*, 2005, **102**, 9133–9137.
16 W. Liu, L. M. Jawerth, E. A. Sparks, M. R. Falvo, R. R. Hantgan, R. Superfine, S. T. Lord and M. Guthold, *Science*, 2006, **313**, 634.
17 H. Kang, Q. Wen, P. A. Janmey, J. X. Tang, E. Conti and F. C. MacKintosh, *J. Phys. Chem. B*, 2009, **113**, 3799–3805.
18 C. Storm, J. J. Pastore, F. C. MacKintosh, T. C. Lubensky and P. A. Janmey, *Nature*, 2005, **435**, 191–194.
19 C. Heussinger and E. Frey, *Phys. Rev. Lett.*, 2006, **97**, 105501.
20 P. Onck, T. Koeman, T. Van Dillen and E. Van der Giessen, *Phys. Rev. Lett.*, 2005, **95**, 178102.
21 N. E. Hudson, J. R. Houser, E. T. O'Brien III, I. Taylor, M. Russell, R. Superfine, S. T. Lord and M. R. Falvo, *Biophys. J.*, 2010, **98**, 1632–1640.
22 A. S. Wolberg, D. M. Monroe, H. R. Roberts and M. Hoffman, *Blood*, 2003, **101**, 3008–3013.
23 G. Késmárky, P. Kenyeres, M. Rábai and K. Tóth, *Clinical. Hemor. Microcirc.*, 2008, **39**, 243–246.
24 P. L. Chandran and V. H. Barocas, *J. Biomech. Eng.*, 2006, **128**, 259–270.
25 P. L. Chandran and V. H. Barocas, *J. Biomech. Eng.*, 2007, **129**, 137–147.
26 T. Stylianopoulos and V. H. Barocas, *J. Biomech. Eng.*, 2007, **129**, 611–618.
27 T. Stylianopoulos, A. Yeckel, J. Derby, X. J. Luo, M. S. Shephard, E. A. Sander and V. H. Barocas, *Phys. Fluids*, 2008, **20**, 123601.
28 R. A. Campbell, K. A. Overmyer, C. H. Selzman, B. C. Sheridan and A. S. Wolberg, *Blood*, 2009, **114**, 4886–4896.
29 Y. Barenholz, D. Gibbes, B. J. Litman, J. Goll, T. E. Thompson and R. D. Carlson, *Biochemistry*, 1977, **16**, 2806–2810.
30 R. Adams and L. Bischof, *IEEE Transactions On Pattern Analysis and Machine Intelligence*, 1994, **16**, 641–647.
31 T. C. Lee, R. L. Kashyap and C. N. Chu, *Cvgip-Graphical Models and Image Processing*, 1994, **56**, 462–478.
32 D. Shaked and A. Bruckstein, *Computer Vision and Image Understanding*, 1998, **69**, 156–169.
33 T. K. Dey and J. Sun, *Proceedings of the 26th International Conference on Foundations of Software Technology and Theoretical Computer Science*, 2006, 21–32.
34 A. S. Wolberg, G. A. Allen, D. M. Monroe, U. Hedner, H. R. Roberts and M. Hoffman, *Br. J. Haemat.*, 2005, **131**, 645–655.
35 S. He, M. Ezban, N. Bark, E. Persson and U. Hedner, *Thromb. Haemostasis*, 2009, **102**, 790–792.
36 K. R. Machlus, J. C. Cardenas, F. C. Church and A. S. Wolberg, *Blood*, 2011, PMID: 21355090.
37 D. F. Brophy, E. J. Martin, M. E. Nolte, J. G. Kuhn and M. E. Carr Jr, *Haemophilia*, 2007, **13**, 533–541.
38 P. Whittaker and K. Przyklenk, *Blood Cells, Molecules, and Diseases*, 2009, **42**, 51–56.
39 R. A. Campbell, M. Aleman, L. D. Gray, M. R. Falvo and A. S. Wolberg, *Thromb. Haemostasis*, 2010, **104**, 1281–1284.

